

Is-NeRF: In-scattering Neural Radiance Field for Blurred Images

Nan Luo^{1*}, Chenglin Ye², Jiaxu Li¹, Gang Liu¹, Bo Wan¹, Di Wang¹, Lupeng Liu², Jun Xiao²

¹Xidian University

²University of the Chinese Academy of Sciences

Abstract

Neural Radiance Fields (NeRF) has gained significant attention for its prominent implicit 3D representation and realistic novel view synthesis capabilities. Available works unexceptionally employ straight-line volume rendering, which struggles to handle sophisticated lightpath scenarios and introduces geometric ambiguities during training, particularly evident when processing motion-blurred images. To address these challenges, this work proposes a novel deblur neural radiance field, Is-NeRF, featuring explicit lightpath modeling in real-world environments. By unifying six common light propagation phenomena through an in-scattering representation, we establish a new scattering-aware volume rendering pipeline adaptable to complex lightpaths. Additionally, we introduce an adaptive learning strategy that enables autonomous determining of scattering directions and sampling intervals to capture finer object details. The proposed network jointly optimizes NeRF parameters, scattering parameters, and camera motions to recover fine-grained scene representations from blurry images. Comprehensive evaluations demonstrate that it effectively handles complex real-world scenarios, outperforming state-of-the-art approaches in generating high-fidelity images with accurate geometric details.

Introduction

The emergence of Neural Radiance Field (Mildenhall et al. 2021) (NeRF) has catalyzed extensive research efforts, driven by its remarkable capability of implicit 3D representation and realistic novel view synthesis. NeRF maps arbitrary continuous 3D coordinates to volume densities and colors via MLPs given a set of posed images, and then generates novel view images via volume rendering. While NeRF has achieved great success in various domains (Barron et al. 2021; Martin-Brualla et al. 2021; Huang et al. 2022; Levy et al. 2023), most variants are trained and tested under meticulously controlled environments with images clearly captured from multiple viewpoints. In real-world scenarios, image data usually contains various forms of degradation or noise, such as motion blur or defocus that degrade image quality, thereby diminishing NeRF’s performance.

Recent studies have explored extending NeRF to address motion-blurred image reconstruction (Ma et al. 2022; Lee et al. 2023; Wang et al. 2023; Qi et al. 2024; Low and Lee

2025), achieving partial improvements in implicit 3D scene representation. However, the presence of non-Lambertian surfaces in real-world scenes (e.g. glasses, metallic materials, and liquid interfaces) brings difficulties to the standard volume rendering paradigm adopted by NeRF-based methods. Due to the light reflection or refraction, the color of spatial point at the surface of medium varies sharply with respect to viewing directions, which corresponds to high frequency property in color variation that can not be precisely learned and expressed by neural networks, resulting in ambiguities in color and geometry during training. Such deficiencies become particularly pronounced under motion blur conditions, where conventional positional encoding techniques prove insufficient to resolve inherent variations in blurred observations. Furthermore, the rigid sampling strategy of NeRF, despite coarse-to-fine design, lacks the adaptability required to preserve geometric details in small-scale objects or thin structures.

In tackling these limitations, this paper attempts to model complex light transport in real-world scenes based on light scattering theory. By simplifying the commonly encountered light propagation phenomena (including reflection, refraction, transmission, glossiness, diffusion) with a generalized in-scattering model, we propose a new scattering-aware volume rendering method and an optimized neural radiance field network for motion blur mitigation. Our network simultaneously learns NeRF parameters, scattering parameters, and camera motions, achieving accurate scene representation in complex scenarios while enhancing the detail-capturing capability. The main contributions of this work are summarized as follows:

- We propose an in-scattering model that integrates common light transports in real-world, and a new volume rendering method which is applicable to light scattering.
- Based on the proposed in-scattering model and volume rendering method, we design an enhanced deblur network, Is-NeRF, for complex real-world scenes.
- We develop a self-guided learning strategy of scattering directions and sampling intervals, achieving high-fidelity scene representation with finer geometric details.
- Extensive experiments on real-world datasets demonstrate Is-NeRF’s effectiveness in handling motion-blurred images and complex light transport scenarios.

*Corresponding author

Related Work

Neural Radiance Field

Owing to its excellent 3D scene representation and novel view synthesis ability, NeRF has been applied to several areas, e.g. scene reconstruction (Li et al. 2021; Sun et al. 2021; Li et al. 2022), 3D generative models (Niemeyer and Geiger 2021; Schwarz et al. 2020), relighting (Philip et al. 2021; Srinivasan et al. 2021), human-body reconstruction (Peng et al. 2021; Su et al. 2021), etc. However, there are few studies aiming at non-ideal conditions. Mip-NeRF (Barron et al. 2021) addresses the aliasing issue of ray sampling, and then Mip-NeRF360 (Barron et al. 2022) expand it to unbounded scenes. NeRF-W (Martin-Brualla et al. 2021) deals with appearance inconsistencies and transient objects in acquired images, HDR-NeRF (Huang et al. 2022) simulates High Dynamic Range radiance to imitate the physical process of image acquisition. SeaThru-NeRF (Levy et al. 2023) proposes a suitable architecture for scene learning in a scattering medium. On the other hand, many methods focus on lifting the rendering efficiency of NeRFs, which are mainly categorized into grid-based (Cao and Johnson 2023; Chen et al. 2022; Fridovich-Keil et al. 2023, 2022) and hash-based (Müller et al. 2022; Wang et al. 2020) methods. Despite these efforts, achieving real-time rendering of unbounded and complete scenes remains challenging. All these methods rely on accurate camera poses and high quality images.

Deblur Neural Radiance Fields

In practice, training accurate neural radiance field from blurry images is more common. Deblur-NeRF (Ma et al. 2022) explores a new area of training neural radiance fields from blurred images end-to-end by simulating blurring kernels to optimize potential sharp images during inference. Luthra et al. (Luthra et al. 2024) propose to learn spatial varying blurring kernels. DP-NeRF (Lee et al. 2023) and Sharp-NeRF (Lee et al. 2024a) enhance the deblurring quality by designing more efficient kernels. However, these methods prefer defocus blur.

Several works have been proposed to deal with motion blur, gratifying results have been obtained for both image deblurring (Kupyn et al. 2019; Tao et al. 2018) and video deblurring (Su et al. 2017). Haesol et al. (Park and Mu Lee 2017) jointly recover camera pose, dense depth map, and potentially sharp images from multi-view motion blurred images. MP-NeRF (Wang et al. 2024) and MBS-NeRF (Gao et al. 2025) introduce depth and prior information. BAD-NeRF (Wang et al. 2023) improves the robustness in intense motion blurred images by explicitly modeling the physical causes of motion blur. Moreover, event-driven methods (Qi et al. 2023, 2024; Low and Lee 2025) for event camera also gain success. ScatterNeRF (Ramazzina et al. 2023) introduces attenuation coefficient to model light scattering in inclement weather conditions, and Aleth-NeRF (Cui et al. 2024) integrates concealing field in volume rendering for low-light & over-exposure. NeRF-based methods employ traditional straight-line sampling, struggle to handle complex light propagation, leading to geometric ambiguities in real-world scenarios. New ideas are expected in this field.

Modeling

In-scattering Lightpath Model

In real-world scenarios with extensive light reflection, refraction, or transmission, the straight-line sampling strategy in standard volume rendering incorrectly interprets images formed by reflected or refracted rays as originating from objects positioned along straight paths, causing inconsistencies between reconstructed property and physical reality. This misguidance would be amplified by motion blurring, hindering convergence to accurate color and geometry.

According to scattering theory, photons from any direction can scatter into the current lightpath and contribute to the final radiance, namely, in-scattering. By analyzing the daily scenarios, we summarize them into six ways of light transportation and unify them as in-scattering (Figure 1 and Appendix A), where lights meet at a point on the medium or surface, with multiple scattered rays converging into the camera’s incident path to form a pixel. This In-scattering Lightpath Model (ISLM) decomposes the complex lightpath into two parts: primary lightpath and scattering lightpath. The sampling points along both parts can be learned and combined to render pixel color.

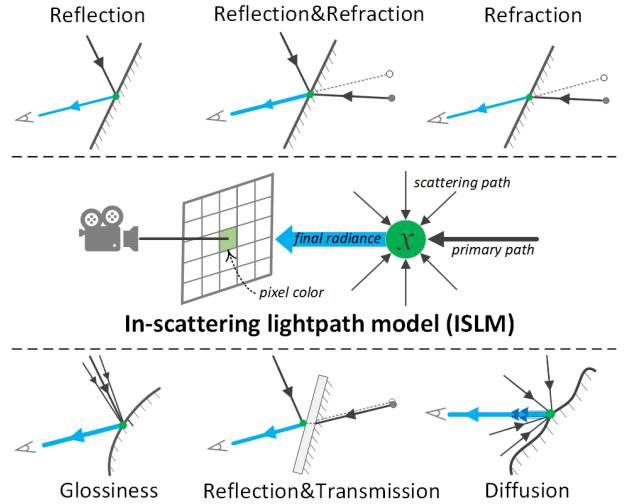


Figure 1: The in-scattering lightpath model (ISLM). It unifies six commonly seen phenomena.

Scattering-aware Volume Rendering

With ISLM generates new sampling points in the scattering directions, the final color of a pixel is then jointly rendered by the volume densities and radiance contributions from all sampling points on both the primary and scattering light-paths. The mathematical formulation of ISLM is defined as:

$$S(\hat{\Theta}) : (\mathbf{x}_t, \mathbf{d}) \rightarrow (\mathbf{d}_s, l) \quad (1)$$

This function maps the spatial coordinates \mathbf{x}_t of a sampling point on the primary path \mathbf{d} to its scattering path \mathbf{d}_s and the sampling interval l . Unlike NeRF’s sampling strategy, ISLM directly controls the sampling interval (see Figure 2)

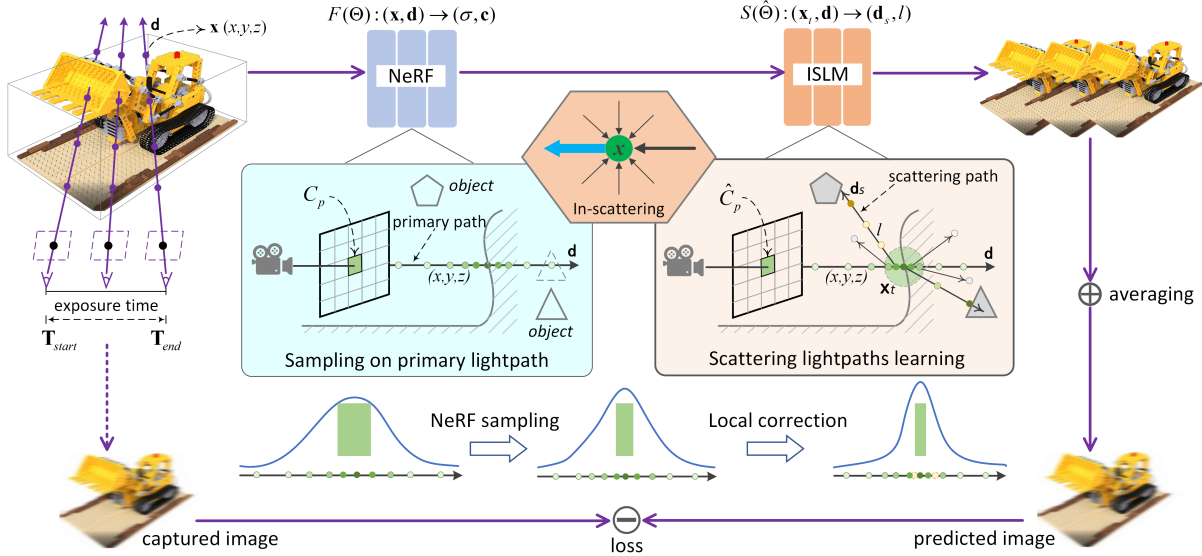


Figure 2: **The pipeline of Is-NeRF.** Given a set of motion blurred images, first we try to learn 3D representations along primary paths ($F(\Theta)$) and camera trajectories in exposure time. Then we propose an In-scattering Lightpath Model (ISLM) and design a scattering-aware volume rendering which are used to learn scattering representations ($S(\hat{\Theta})$) and to render virtual sharp images. During this process, the local density of sampling points is corrected to capture better details. The blurry image is synthesized by averaging those virtual images and used to construct photo-metric loss for network training.

to regulate the length of scattering path. The coordinates of sampling points along scattering path are computed by Eq. (2), where x_{tj} denotes the j -th sample on scattering path d_s originated from x_t , N_t is the number of sampling points.

$$x_{tj} = x_t + j \cdot l \cdot d_s, \quad j \in \{1, 2, \dots, N_t\} \quad (2)$$

Then, the final pixel color \hat{C}_p integrates contributions from both the primary and scattering paths. The equation of volume rendering is extended as follows:

$$\hat{C}_p = C_p + \sum_{k=1}^K \sum_{i=1}^{N_k} T_{ki} (1 - \exp(-\sigma_{ki} l_k)) c_{ki} \quad (3)$$

$$T_{ki} = \exp \left(- \sum_{j=1}^{i-1} \sigma_{kj} \delta_{kj} \right) \quad (4)$$

Here, C_p means the color contribution along primary path. K and N_k are parameters controlling the number of scattering paths and sampling points per path, respectively. σ_{ki} and c_{ki} represent the volume density and color at the i -th sample on the k -th scattering path. T_{ki} acts as a path validity mask: for incorrectly predicted paths, T_{ki} suppresses their contribution to the final color, ensuring ISLM converges to physically accurate lightpaths.

Framework

By integrating ISLM, we propose a new framework, named Is-NeRF, to deal with blurred images. It jointly optimizes NeRF parameters, ISLM parameters and camera trajectories, progressively refining ideal straight-line sampling into physically accurate scattering lightpaths to adapt various real-world scenes. Figure 2 illustrate the overall structure.

Network pipeline

There are four main steps: (1) Camera pose interpolation. Linearly interpolate between the initial pose T_{start} and the final pose T_{end} in $SE(3)$ space to generate sampling moments and corresponding virtual camera poses (see Appendix A). (2) Primary path sampling. Follow NeRF's coarse-to-fine strategy to predict color and density ($F(\Theta)$) at spatial sampling points along primary lightpath. (3) ISLM-guided scattering learning. Taking primary path and the chosen sampling point as input, ISLM then learns scattering directions d_s and sampling intervals l grow from the primary point ($S(\hat{\Theta})$). (4) Blur synthesis and optimization. Render virtual sharp images for each sampling moment by Eq. (3), average them to predict motion-blurred images, and minimize the photometric error between predicted and input blurred images. The NeRF parameters Θ , ISLM parameters $\hat{\Theta}$, as well as T_{start} and T_{end} are jointly optimized.

Adaptive Sampling of ISLM

Determining scattering lightpaths and their sampling points is critical to ISLM and the network. Theoretically, multiple scattering paths should originate from the intersection of the primary lightpath and object surface, with sampling points generated according to NeRF's sampling principles. By parameter adjustments, the network would gradually converge to accurate paths. However, selecting sole intersection point in practice is overly idealized (sampling points on primary path themselves are statistically estimated) and contradicts the principles of volume rendering, thereby can not guarantee robustness. Inspired by ray-tracing optimization, this work constructs scattering paths from adjacent sam-

pling points along the primary path and assigns each point one scattering path to collectively simulate light scattering. There are three key things: (1) The quantity of scattering paths. Five primary points are selected to grow scattering paths, which jointly simulate the scattering locations and global effects (see Figure 2). (2) Scattering direction. By fixing the count of primary points and scattering paths, the network adaptively learns the direction \mathbf{d}_s of each path, ensuring convergence of all paths. (3) Sampling along scattering path. To balance training efficiency and precision, we employ fixed-number equidistant sampling on scattering paths, where interval l is another learnable parameter.

Local Density Correction

NeRF’s hierarchical sampling strategy relies heavily on the initial sampling of coarse network. When small objects occupy the space, most samples may fall off the object and cause the bandwidth of peak of probability density to expand. This forces the network to adjust parameters of adjacent points to approximate the true geometry. The intended probability density peak is averaged across neighboring samples, leading to inaccurate geometric representations. Is-NeRF addresses this issue by generating network-controlled scattering lightpaths through ISLM. These scattering paths increase the probability of sampling points hitting small objects. Moreover, the intervals along scattering paths are learned by the network and jointly optimized with other parameters, enabling adaptive adjustments. This strategy enhances Is-NeRF’s perception of fine structures compared to prior methods, as validated by experimental results.

Loss Function

Given M motion-blurred images, our method can jointly optimize the parameters of ISLM ($\hat{\Theta}$), NeRF (Θ), and the camera motion trajectories (i.e., $\mathbf{T}_{\text{start}}$ and \mathbf{T}_{end}) by minimizing the photometric loss which is formulated as:

$$\mathcal{L} = \sum_{m=1}^M \sum_{\mathbf{x}} \left\| \hat{B}_m(\mathbf{x}) - B_m^{\text{gt}}(\mathbf{x}) \right\|_2^2 \quad (5)$$

where $\hat{B}_m(\mathbf{x})$ is the motion-blurred image predicted by Is-NeRF, and $B_m^{\text{gt}}(\mathbf{x})$ denotes the captured blurring image. The following Jacobian matrices are required to update parameters via stochastic gradient descent.

$$\frac{\partial \mathcal{L}}{\partial \hat{\Theta}} = \sum_{m=1}^M \frac{\partial \mathcal{L}}{\partial B_m(\mathbf{x})} \cdot \frac{1}{n} \sum_{i=1}^n \frac{\partial B_m(\mathbf{x})}{\partial \hat{C}_i} \cdot \frac{\partial \hat{C}_i}{\partial \hat{\Theta}} \quad (6)$$

$$\frac{\partial \mathcal{L}}{\partial \Theta} = \sum_{m=1}^M \frac{\partial \mathcal{L}}{\partial B_m(\mathbf{x})} \cdot \frac{1}{n} \sum_{i=1}^n \frac{\partial B_m(\mathbf{x})}{\partial \hat{C}_i} \cdot \frac{\partial \hat{C}_i}{\partial \Theta} \quad (7)$$

$$\frac{\partial \mathcal{L}}{\partial \mathbf{T}_{\text{start}}} = \sum_{m=1}^M \frac{\partial \mathcal{L}}{\partial B_m(\mathbf{x})} \cdot \frac{1}{n} \sum_{i=1}^n \frac{\partial B_m(\mathbf{x})}{\partial \hat{C}_i} \cdot \frac{\partial \hat{C}_i}{\partial \mathbf{T}_{\text{start}}} \quad (8)$$

$$\frac{\partial \mathcal{L}}{\partial \mathbf{T}_{\text{end}}} = \sum_{m=1}^M \frac{\partial \mathcal{L}}{\partial B_m(\mathbf{x})} \cdot \frac{1}{n} \sum_{i=1}^n \frac{\partial B_m(\mathbf{x})}{\partial \hat{C}_i} \cdot \frac{\partial \hat{C}_i}{\partial \mathbf{T}_{\text{end}}} \quad (9)$$

Experimental Evaluation

We conduct parameter evaluations, comparative evaluations, and ablation studies on two datasets: a public motion-blurred dataset provided by Deblur-NeRF (Ma et al. 2022) and a self-captured dataset. All experiments are conducted on a NVIDIA RTX3090 GPU (24GB). The rendered images are evaluated in three metrics: PSNR, SSIM, and LPIPS.

Parameter Evaluations

The number of primary points initiating scattering N_k critically influence Is-NeRF’s performance. Theoretically, larger N_k corresponds to finer detail modeling and better handling of light scattering. However, excessive N_k hinders convergence of model and reduces efficiency. Conversely, insufficient N_k fails to adequately model light scattering, degrading performance. Figure 3 shows the PSNR and training time for scene ‘Pool’ and ‘Cozy2Room’ across varying N_k . Results reveal that $N_k = 5$, originating scattering paths from five adjacent primary points, balances accuracy and efficiency, while excessive N_k only inflates training time without improving image quality.

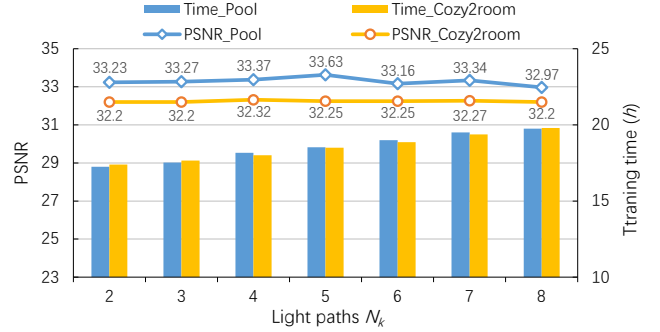


Figure 3: The PSNR and training time under varying number of scattering lightpaths N_k .

Scene	5 rays at 1 point			1 ray at each of 5 points		
	PSNR↑	SSIM↑	LPIPS↓	PSNR↑	SSIM↑	LPIPS↓
Cozy2room	28.77	0.8598	0.1443	32.25	0.9162	0.0515
Pool	27.83	0.7128	0.3539	33.53	0.8962	0.0749
Bottle	23.19	0.8240	0.3293	23.89	0.9403	0.0836
LakeCorner	25.54	0.6926	0.4091	27.14	0.7780	0.3013

Table 1: Quantitative comparison of two scattering designs. It is evident that the second design prevails in all metrics.

Additionally, we compare two scattering designs: 1) emitting five rays from a single primary sampling point, versus 2) emitting one scattering ray from each of five adjacent primary points. The results in Table 1 show that emitting rays from five consecutive primary points outperforms the single-point multi-ray style (Intuitive results given in Appendix B also support this conclusion). This aligns with the principle of volume rendering that more scattering origins increase the likelihood of capturing true scattering locations. Based on these findings, we adopt the second design, prioritizing scattering path diversity over single-point multiplicity.

Method	Cozy2room			Factory			Pool			Tanabata			Trolley		
	PSNR↑	SSIM↑	LPIPS↓	PSNR↑	SSIM↑	LPIPS↓	PSNR↑	SSIM↑	LPIPS↓	PSNR↑	SSIM↑	LPIPS↓	PSNR↑	SSIM↑	LPIPS↓
NeRF (2021)	25.66	0.7941	0.2288	19.32	0.4563	0.5304	30.45	0.8354	0.1932	22.22	0.6807	0.3653	21.25	0.6370	0.3633
MPR (2021)	29.90	0.8862	0.0915	25.07	0.6940	0.2409	33.28	0.8938	0.1290	22.60	0.7203	0.2507	26.24	0.8356	0.1762
PVD (2021)	28.06	0.8443	0.1515	24.57	0.6877	0.3150	30.38	0.8393	0.1977	22.54	0.6872	0.3351	24.44	0.7746	0.2600
SRN-Deblur (2018)	29.47	0.8759	0.0950	26.54	0.7604	0.2404	32.94	0.8847	0.1045	23.20	0.7274	0.2438	25.36	0.8119	0.1618
Deblur-NeRF (2022)	25.96	0.7979	0.1024	23.21	0.6487	0.2618	31.21	0.8518	0.1382	22.46	0.6946	0.2455	24.94	0.7923	0.1766
DP-NeRF (2023)	30.77	0.9020	0.0584	27.69	0.8328	0.1847	33.22	0.8922	0.0954	25.27	0.7973	0.1779	26.99	0.8413	0.1312
Sharp-NeRF (2024)	25.65	0.7994	0.2322	19.78	0.4498	0.4596	30.53	0.8520	0.1845	18.12	0.4609	0.4633	21.67	0.6992	0.3073
MP-NeRF (2024)	32.49	0.9296	0.0368	28.45	0.8497	0.1629	31.30	0.8641	0.1029	27.82	0.8821	0.0872	28.67	0.8832	0.0854
BAD-NeRF (2023)	32.15	0.9139	0.0527	32.13	0.9106	0.1219	32.22	0.8600	0.0908	27.76	0.8600	0.1195	29.25	0.8892	0.0833
3DGS (2023)	25.59	0.8076	0.1645	18.11	0.4179	0.4958	25.63	0.6326	0.2632	21.35	0.6686	0.3235	20.56	0.6257	-
Deblurring-3DGS (2024)	31.45	0.9222	0.0367	24.01	0.7333	0.2326	31.87	0.8829	0.0751	27.01	0.8807	0.0785	26.88	0.8710	-
Is-NeRF (ours)	32.25	0.9162	0.0515	32.31	0.9154	0.1181	33.53	0.8962	0.0749	27.87	0.8614	0.1191	29.27	0.8894	0.0787

Table 2: Quantitative results on Deblur-NeRF dataset. The data reveal that our Is-NeRF achieves the best performance, especially on scene 'Pool' with extensive scatterings. MP-NeRF excels on 'Cozy2room', and BAD-NeRF show its deblur ability.



Figure 4: Intuitive results on Deblur-NeRF dataset, with **local regions enlarged and PSNR given**. The qualitative results show the advantage of our method in detail capturing.

Comparison with SOTA methods

We compare the proposed method with SOTA deblurring NeRF approaches (SRN-Deblur (Tao et al. 2018), PVD (Son et al. 2021), MPR (Zamir et al. 2021), Deblur-NeRF (Ma et al. 2022), DP-NeRF (Lee et al. 2023), Sharp-NeRF (Lee et al. 2024a), MP-NeRF (Wang et al. 2024), baseline BAD-NeRF (Wang et al. 2023)), as well as 3DGS (Kerbl et al. 2023) and Deblurring-3DGS (Lee et al. 2024b), emphasizing its ability to learn local details and scattering lightpaths.

Results on Deblur-NeRF Dataset The public Deblur-NeRF dataset contains five scenes: four (Cozy2Room, Factory, Tanabata, and Trolley) with typical indoor/outdoor diffuse reflections, and one (Pool) with light reflection and refraction. All methods take blurred images as input. Quantitative results are summarized in Table 2. Results reveal that Is-NeRF achieves significant improvements over single-view deblurring approaches (SRNDeblur, PVD, MPR) which rely on limited information from single view. Compared with

Method	Bottle			LakeCorner			Car			Table		
	PSNR \uparrow	SSIM \uparrow	LPIPS \downarrow	PSNR \uparrow	SSIM \uparrow	LPIPS \downarrow	PSNR \uparrow	SSIM \uparrow	LPIPS \downarrow	PSNR \uparrow	SSIM \uparrow	LPIPS \downarrow
NeRF (2021)	20.72	0.7582	0.4113	11.36	0.4067	0.7899	28.36	0.8489	0.2403	25.39	0.7887	0.2600
SRN-Deblur (2018)	29.86	0.9288	0.1107	25.55	0.7150	0.3855	30.20	0.8790	0.1743	26.10	0.8103	0.2242
Deblur-NeRF (2022)	18.72	0.8552	0.1788	19.88	0.5833	0.3295	29.50	0.8806	0.1203	28.63	0.8871	0.1078
DP-NeRF (2023)	22.67	0.9038	0.1047	18.55	0.5390	0.3456	29.99	0.8974	0.0853	29.02	0.8949	0.1052
MP-NeRF (2024)	21.93	0.8802	0.1211	18.56	0.5635	0.3574	29.65	0.8830	0.1012	29.00	0.8847	0.0921
BAD-NeRF (2023)	23.32	0.7857	0.2203	26.56	0.6892	0.3048	31.86	0.9041	0.0912	30.95	0.9093	0.0710
Is-NeRF (ours)	23.89	0.9403	0.0836	27.14	0.7780	0.3013	31.94	0.9048	0.0900	31.20	0.9142	0.0652

Table 3: Quantitative results on self-captured dataset with complex light propagation. The results reveal that our method achieves the best deblur ability in real-world scenarios.

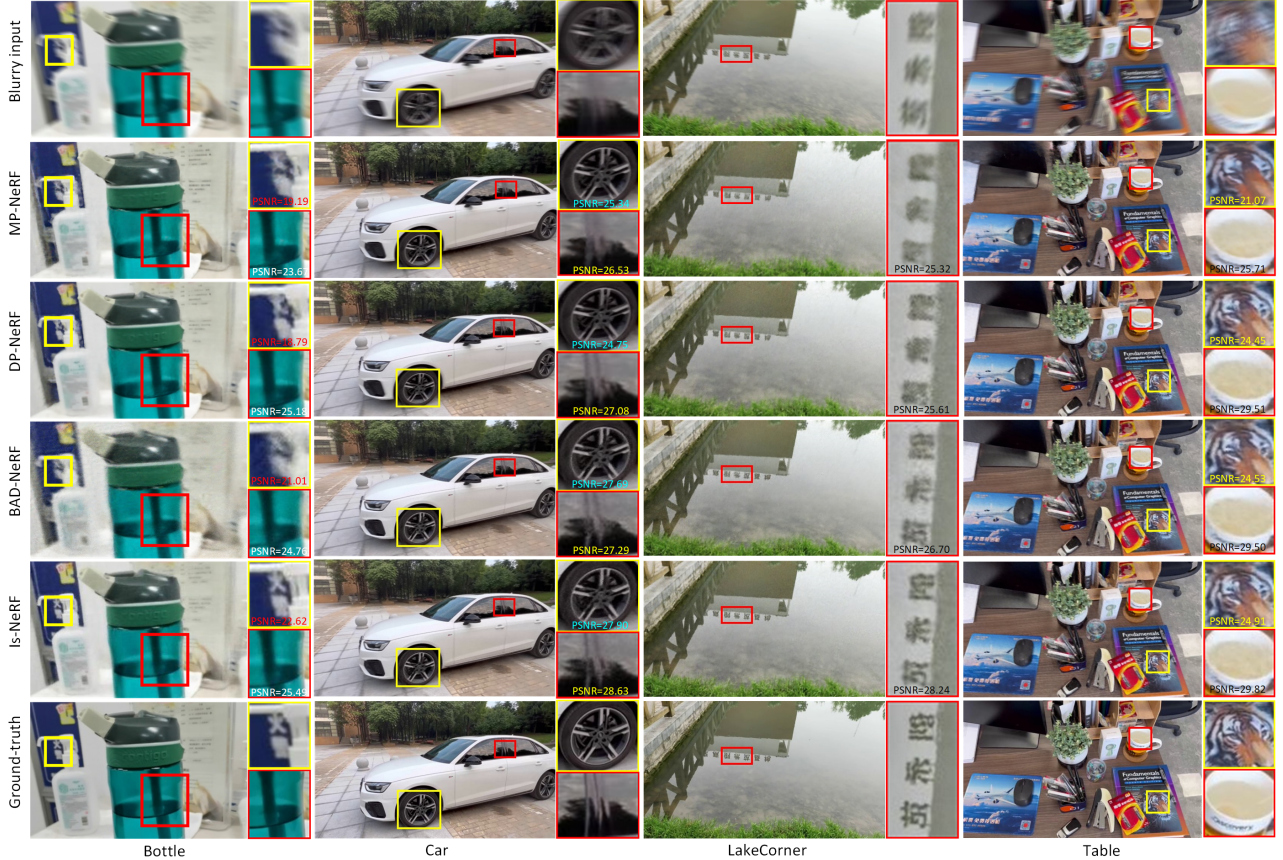


Figure 5: Intuitive results on self-captured dataset, with **local regions enlarged and PSNR given**. The results show that our method outperforms other method on real-world complex scenarios with extensive scatterings.

Deblur-NeRF (Ma et al. 2022), our method outperforms owing to its physics-aware motion blur synthesis. Deblur-NeRF neglects the critical role of camera trajectories in motion blur formation. MP-NeRF (Wang et al. 2024) shows great potential but lacks of adaptability. By introducing scattering paths and local density correction under the scattering-aware volume rendering, Is-NeRF enhances learning ability of subtle geometric details comparing to baseline BAD-NeRF (Wang et al. 2023). This leads to consistent performance gains in ‘Cozy2Room’, ‘Factory’, ‘Tanabata’, and ‘Trolley’. For scene ‘Pool’ (rich in reflection and refraction), the improvement is particularly pronounced, validating the

ISLM’s ability to model scattering light transport and correct errors from straight-path sampling.

We also intuitively show the results in Figure 4. Take ‘Pool’ as example, red box highlights large objects without light scattering, where Is-NeRF performs similarly to BAD-NeRF. Yellow box marks water area with more light reflection and refraction, where Is-NeRF outperforms BAD-NeRF, producing sharper and more detailed images. For other scenes with fine textures and geometric structures, Is-NeRF also achieves superior results through local volume density correction. These visual comparisons validate the effectiveness of our scattering-aware rendering.

Method	ISLM		Cozy2room			Factory			Pool			Tanabata		
	Training	Rendering	PSNR \uparrow	SSIM \uparrow	LPIPS \downarrow	PSNR \uparrow	SSIM \uparrow	LPIPS \downarrow	PSNR \uparrow	SSIM \uparrow	LPIPS \downarrow	PSNR \uparrow	SSIM \uparrow	LPIPS \downarrow
Baseline	×	×	32.15	0.9139	0.0527	32.13	0.9106	0.1219	33.10	0.8864	0.0802	27.76	0.8600	0.1195
Is-NeRF	×	✓	13.24	0.4270	0.6393	14.73	0.6393	0.4914	32.97	0.8950	0.0781	18.62	0.7688	0.1896
Is-NeRF	✓	×	29.31	0.8958	0.0873	29.96	0.8996	0.1288	33.51	0.8962	0.0749	27.86	0.8614	0.1192
Is-NeRF	✓	✓	32.25	0.9162	0.0515	32.31	0.9154	0.1181	33.53	0.8962	0.0749	27.87	0.8614	0.1191

Method	ISLM		Bottle			LakeCorner			Car			Table		
	Training	Rendering	PSNR \uparrow	SSIM \uparrow	LPIPS \downarrow	PSNR \uparrow	SSIM \uparrow	LPIPS \downarrow	PSNR \uparrow	SSIM \uparrow	LPIPS \downarrow	PSNR \uparrow	SSIM \uparrow	LPIPS \downarrow
Baseline	×	×	23.32	0.7857	0.2203	26.56	0.6892	0.3048	31.86	0.9041	0.0912	30.95	0.9093	0.0710
Is-NeRF	×	✓	22.64	0.8603	0.2515	26.61	0.7062	0.3053	31.90	0.8979	0.0912	31.08	0.8961	0.0673
Is-NeRF	✓	×	23.67	0.8313	0.0924	27.02	0.7075	0.3005	31.36	0.8936	0.0977	31.20	0.8964	0.0655
Is-NeRF	✓	✓	23.89	0.9403	0.0836	27.14	0.7780	0.3013	31.94	0.9048	0.0900	31.20	0.9142	0.0652

Table 4: The quantitative results of ablation studies of ISLM module to the proposed framework.

Results on self-captured dataset To further validate the advantages of the proposed Is-NeRF, we constructs a dataset featuring complex light transport by capturing real-life scenes. The comparative results are recorded in Table 3. The results show that our Is-NeRF outperforms comparison methods across all three metrics, except that DP-NeRF (Lee et al. 2023) attains the best LPIPS metric for the scene ‘Car’. Deblur-NeRF (Ma et al. 2022) and DP-NeRF exhibit significantly weaker performance in scenes with substantial refraction and reflection (Bottle, LakeCorner, Car) compared to other methods. For the indoor scene ‘Table’, SRN-Deblur and Deblur-NeRF produce inferior results. BAD-NeRF, which directly adopts NeRF’s renderer and straight-line sampling, fails to adapt realistic light propagation. Consequently, it struggles to learn accurate geometric information in scenes with extensive light scattering, also validated by the qualitative results.

To intuitively express Is-NeRF’s enhancements in detail learning and scattering lightpath representing, we present image synthesis results in Figure 5, highlighting local regions and the PSNR values. Scene ‘Car’ contains reflections from glass surfaces and car paint, while ‘LakeCorner’ features large-scale regions with fraction and reflection. Our method demonstrate superior representation of such scenarios, recovering finer local details and achieving higher local PSNR comparing to other methods. For ‘Table’ scene, which includes glossy highlights (e.g., book cover) and refraction, our method also delivers the best visual representation. Scene ‘Bottle’ contains image textures and transmission effects. It is evident that Is-NeRF captures more details compared to BAD-NeRF. Additionally, Is-NeRF excels in modeling light transmission: the straw inside, objects behind the bottle, and shadow contours on the table are rendered with significantly clearer definition.

The above results demonstrate that the proposed in-scattering lightpath model and the extended volume rendering handles sophisticated light transport effectively and can recover sharper scene details. This approach robustly adapts to diverse real-world scenarios, showcasing superior generalizability and applicability.

Ablation Studies

To investigate ISLM’s contribution to Is-NeRF, we conduct ablation studies. Removing ISLM from training implies

disabling scattering path learning and local density correction, while removing ISLM from rendering retains scattering paths learned during training but performs standard volume rendering. If learning scattering lightpaths is unnecessary, removing ISLM module will not make noticeable difference.

As the data in Table 4 reveals, removing the ISLM module significantly degrades synthesis quality on Deblur-NeRF dataset. For ‘Cozy2Room’, ‘Factory’, and ‘Tanabata’, removing ISLM during training causes substantial performance degradation. For ‘Pool’ and self-captured scenes, the performance also declines moderately, though the model’s overall deblurring capability remains superior to the baseline BAD-NeRF. Removing ISLM during rendering has a slightly smaller impact, with similar trends observed across both datasets. Intuitive comparisons are given in Appendix C. These results reveal that ISLM plays a decisive role during the training: it corrects sampling rays to align with the true lightpaths and enables Is-NeRF to learn sufficient geometric information via local density correction. The promotion benefits from ISLM in training outweigh the loss caused by disabling it during rendering. This is critical for scenarios with rich reflection or refraction, where ISLM’s ability to gain physically consistent sampling is indispensable.

Conclusion

This work presents a new neural radiance field framework Is-NeRF to learn finer 3D representations of real-world scenes with sophisticated lightpaths from motion blurred images. We unify six daily seen light transport phenomena with an in-scattering model and propose an extended scattering-aware volume rendering method. Based on the theoretical modeling, a network that can adaptively learn scattering paths to optimize scene representations is designed, with local density correction ability to obtain accurate geometric details. Extensive experiments on synthetic and self-captured datasets then verify its superiority and applicability in complex real-life scenarios.

This work brings new thoughts to neural radiance field and volume rendering. In the future, we will try to strike a balance between accuracy and speed by utilizing more efficient architectures (such as Zip-NeRF, Instant-NGP) as backbone. Another promising direction is to extend the in-scattering model to 3D Gaussian Splatting related fields.

References

- Barron, J. T.; Mildenhall, B.; Tancik, M.; Hedman, P.; Martin-Brualla, R.; and Srinivasan, P. P. 2021. Mip-nerf: A multiscale representation for anti-aliasing neural radiance fields. In *Proceedings of the IEEE/CVF International Conference on Computer Vision*, 5855–5864.
- Barron, J. T.; Mildenhall, B.; Verbin, D.; Srinivasan, P. P.; and Hedman, P. 2022. Mip-nerf 360: Unbounded anti-aliased neural radiance fields. In *Proceedings of the IEEE/CVF Conference on Computer Vision and Pattern Recognition*, 5470–5479.
- Cao, A.; and Johnson, J. 2023. Hexplane: A fast representation for dynamic scenes. In *Proceedings of the IEEE/CVF Conference on Computer Vision and Pattern Recognition*, 130–141.
- Chen, A.; Xu, Z.; Geiger, A.; Yu, J.; and Su, H. 2022. Tensorf: Tensorial radiance fields. In *European conference on computer vision*, 333–350. Springer.
- Cui, Z.; Gu, L.; Sun, X.; Ma, X.; Qiao, Y.; and Harada, T. 2024. Aleth-NeRF: Illumination Adaptive NeRF with Concealing Field Assumption.
- Fridovich-Keil, S.; Meanti, G.; Warburg, F. R.; Recht, B.; and Kanazawa, A. 2023. K-planes: Explicit radiance fields in space, time, and appearance. In *Proceedings of the IEEE/CVF Conference on Computer Vision and Pattern Recognition*, 12479–12488.
- Fridovich-Keil, S.; Yu, A.; Tancik, M.; Chen, Q.; Recht, B.; and Kanazawa, A. 2022. Plenoxels: Radiance fields without neural networks. In *Proceedings of the IEEE/CVF conference on computer vision and pattern recognition*, 5501–5510.
- Gao, C.; Sun, Q.; Zhu, J.; and Chen, J. 2025. MBS-NeRF: reconstruction of sharp neural radiance fields from motion-blurred sparse images. *Scientific Reports*, 15(1).
- Huang, X.; Zhang, Q.; Feng, Y.; Li, H.; Wang, X.; and Wang, Q. 2022. Hdr-nerf: High dynamic range neural radiance fields. In *Proceedings of the IEEE/CVF Conference on Computer Vision and Pattern Recognition*, 18398–18408.
- Kerbl, B.; Kopanas, G.; Leimkühler, T.; and Drettakis, G. 2023. 3d gaussian splatting for real-time radiance field rendering. *ACM Trans. Graph.*, 42(4): 139–1.
- Kupyn, O.; Martyniuk, T.; Wu, J.; and Wang, Z. 2019. Deblurgan-v2: Deblurring (orders-of-magnitude) faster and better. In *Proceedings of the IEEE/CVF international conference on computer vision*, 8878–8887.
- Lee, B.; Lee, H.; Ali, U.; and Park, E. 2024a. Sharp-NeRF: Grid-Based Fast Deblurring Neural Radiance Fields Using Sharpness Prior. In *Proceedings of the IEEE/CVF Winter Conference on Applications of Computer Vision (WACV)*, 3709–3718.
- Lee, B.; Lee, H.; Sun, X.; Ali, U.; and Park, E. 2024b. Deblurring 3D Gaussian Splatting. arXiv:2401.00834.
- Lee, D.; Lee, M.; Shin, C.; and Lee, S. 2023. Dp-nerf: Deblurred neural radiance field with physical scene priors. In *Proceedings of the IEEE/CVF Conference on Computer Vision and Pattern Recognition*, 12386–12396.
- Levy, D.; Peleg, A.; Pearl, N.; Rosenbaum, D.; Akkaynak, D.; Korman, S.; and Treibitz, T. 2023. Seathru-nerf: Neural radiance fields in scattering media. In *Proceedings of the IEEE/CVF Conference on Computer Vision and Pattern Recognition*, 56–65.
- Li, T.; Slavcheva, M.; Zollhoefer, M.; Green, S.; Lassner, C.; Kim, C.; Schmidt, T.; Lovegrove, S.; Goesele, M.; Newcombe, R.; et al. 2022. Neural 3d video synthesis from multi-view video. In *Proceedings of the IEEE/CVF Conference on Computer Vision and Pattern Recognition*, 5521–5531.
- Li, Z.; Niklaus, S.; Snavely, N.; and Wang, O. 2021. Neural scene flow fields for space-time view synthesis of dynamic scenes. In *Proceedings of the IEEE/CVF Conference on Computer Vision and Pattern Recognition*, 6498–6508.
- Low, W. F.; and Lee, G. H. 2025. Deblur e-NeRF: NeRF from Motion-Blurred Events under High-speed or Low-light Conditions. In *European Conference on Computer Vision*.
- Luthra, A.; Gantha, S. S.; Song, X.; Yu, H.; Lin, Z.; and Peng, L. 2024. Deblur-NSFF: Neural Scene Flow Fields for Blurry Dynamic Scenes. In *Proceedings of the IEEE/CVF Winter Conference on Applications of Computer Vision*, 3658–3667.
- Ma, L.; Li, X.; Liao, J.; Zhang, Q.; Wang, X.; Wang, J.; and Sander, P. V. 2022. Deblur-nerf: Neural radiance fields from blurry images. In *Proceedings of the IEEE/CVF Conference on Computer Vision and Pattern Recognition*, 12861–12870.
- Martin-Brualla, R.; Radwan, N.; Sajjadi, M. S.; Barron, J. T.; Dosovitskiy, A.; and Duckworth, D. 2021. Nerf in the wild: Neural radiance fields for unconstrained photo collections. In *Proceedings of the IEEE/CVF Conference on Computer Vision and Pattern Recognition*, 7210–7219.
- Mildenhall, B.; Srinivasan, P. P.; Tancik, M.; Barron, J. T.; Ramamoorthi, R.; and Ng, R. 2021. Nerf: Representing scenes as neural radiance fields for view synthesis. *Communications of the ACM*, 65(1): 99–106.
- Müller, T.; Evans, A.; Schied, C.; and Keller, A. 2022. Instant neural graphics primitives with a multiresolution hash encoding. *ACM transactions on graphics (TOG)*, 41(4): 1–15.
- Niemeyer, M.; and Geiger, A. 2021. Giraffe: Representing scenes as compositional generative neural feature fields. In *Proceedings of the IEEE/CVF Conference on Computer Vision and Pattern Recognition*, 11453–11464.
- Park, H.; and Mu Lee, K. 2017. Joint estimation of camera pose, depth, deblurring, and super-resolution from a blurred image sequence. In *Proceedings of the IEEE International Conference on Computer Vision*, 4613–4621.
- Peng, S.; Dong, J.; Wang, Q.; Zhang, S.; Shuai, Q.; Zhou, X.; and Bao, H. 2021. Animatable neural radiance fields for modeling dynamic human bodies. In *Proceedings of the IEEE/CVF International Conference on Computer Vision*, 14314–14323.
- Philip, J.; Morgenthaler, S.; Gharbi, M.; and Drettakis, G. 2021. Free-viewpoint indoor neural relighting from multi-view stereo. *ACM Transactions on Graphics (TOG)*, 40(5): 1–18.

Qi, Y.; Zhu, L.; Zhang, Y.; and Li, J. 2023. E2NeRF: Event Enhanced Neural Radiance Fields from Blurry Images. In *Proceedings of the IEEE/CVF International Conference on Computer Vision (ICCV)*, 13254–13264.

Qi, Y.; Zhu, L.; Zhao, Y.; Bao, N.; and Li, J. 2024. Deblurring Neural Radiance Fields with Event-driven Bundle Adjustment. In *Proceedings of the 32nd ACM International Conference on Multimedia, MM '24*, 9262–9270. New York, NY, USA: Association for Computing Machinery. ISBN 9798400706868.

Ramazzina, A.; Bijelic, M.; Walz, S.; Sanvito, A.; Scheuble, D.; and Heide, F. 2023. ScatterNeRF: Seeing Through Fog with Physically-Based Inverse Neural Rendering. arXiv:2305.02103.

Schwarz, K.; Liao, Y.; Niemeyer, M.; and Geiger, A. 2020. Graf: Generative radiance fields for 3d-aware image synthesis. *Advances in Neural Information Processing Systems*, 33: 20154–20166.

Son, H.; Lee, J.; Lee, J.; Cho, S.; and Lee, S. 2021. Recurrent video deblurring with blur-invariant motion estimation and pixel volumes. *ACM Transactions on Graphics (TOG)*, 40(5): 1–18.

Srinivasan, P. P.; Deng, B.; Zhang, X.; Tancik, M.; Mildenhall, B.; and Barron, J. T. 2021. Nerv: Neural reflectance and visibility fields for relighting and view synthesis. In *Proceedings of the IEEE/CVF Conference on Computer Vision and Pattern Recognition*, 7495–7504.

Su, S.; Delbracio, M.; Wang, J.; Sapiro, G.; Heidrich, W.; and Wang, O. 2017. Deep video deblurring for hand-held cameras. In *Proceedings of the IEEE conference on computer vision and pattern recognition*, 1279–1288.

Su, S.-Y.; Yu, F.; Zollhöfer, M.; and Rhodin, H. 2021. A-nerf: Articulated neural radiance fields for learning human shape, appearance, and pose. *Advances in Neural Information Processing Systems*, 34: 12278–12291.

Sun, J.; Xie, Y.; Chen, L.; Zhou, X.; and Bao, H. 2021. Neuralrecon: Real-time coherent 3d reconstruction from monocular video. In *Proceedings of the IEEE/CVF conference on computer vision and pattern recognition*, 15598–15607.

Tao, X.; Gao, H.; Shen, X.; Wang, J.; and Jia, J. 2018. Scale-recurrent network for deep image deblurring. In *Proceedings of the IEEE conference on computer vision and pattern recognition*, 8174–8182.

Wang, D.; Wang, Q.; He, L.; Gao, X.; and Tian, Y. 2020. Joint and individual matrix factorization hashing for large-scale cross-modal retrieval. *Pattern recognition*, 107: 107479.

Wang, P.; Zhao, L.; Ma, R.; and Liu, P. 2023. Bad-nerf: Bundle adjusted deblur neural radiance fields. In *Proceedings of the IEEE/CVF Conference on Computer Vision and Pattern Recognition*, 4170–4179.

Wang, X.; Yin, Z.; Zhang, F.; Feng, D.; and Wang, Z. 2024. MP-NeRF: More refined deblurred neural radiance field for 3D reconstruction of blurred images. *Knowledge-based systems*, 290(Apr.22): 1.1–1.10.

Zamir, S. W.; Arora, A.; Khan, S.; Hayat, M.; Khan, F. S.; Yang, M.-H.; and Shao, L. 2021. Multi-stage progressive image restoration. In *Proceedings of the IEEE/CVF conference on computer vision and pattern recognition*, 14821–14831.

Appendix A

Neural Radiance field

As an implicit 3D scene representation method, NeRF centers on using a deep neural network to model the radiance intensity and density at each point in a scene, synthesizing images through volume rendering. Training NeRF typically requires multiple high-quality 2D images and their corresponding camera parameters. It maps the 3D coordinates of a point $\mathbf{x} = (x, y, z)$ and the viewing direction $\mathbf{d} = (\theta, \phi)$ to the view-invariant volume density σ and the view-dependent color $\mathbf{c} = (r, g, b)$:

$$F(\Theta) : (\mathbf{x}, \mathbf{d}) \rightarrow (\sigma, \mathbf{c}) \quad (10)$$

Subsequently, an approximate volume rendering method predicts the color C_p of each pixel using the predicted color \mathbf{c}_i and density σ_i by the NeRF backbone network at each sampled point \mathbf{r}_i along the ray. The coloring equation is expressed as Eq. 11, where T_i denotes the accumulated transmittance and δ_i is the sampling interval.

$$C_p = \sum_{i=1}^N T_i (1 - \exp(-\sigma_i \delta_i)) \mathbf{c}_i, \quad (11)$$

$$T_i = \exp \left(- \sum_{j=1}^{i-1} \sigma_j \delta_j \right) \quad (12)$$

BAD-NeRF

Unlike existing works (e.g., Deblur NeRF) that treat blurred images as the convolution of sharp images with blur kernels, BAD-NeRF analyzes the physical formation process of motion blur. It posits that relative motion between objects and the camera during exposure time causes variations in captured radiance distributions across moments, ultimately manifesting as motion blur. The mathematical model can be approximated as:

$$B(\mathbf{x}) \approx \frac{1}{n} \sum_{t=1}^n I_t(\mathbf{x}) \quad (13)$$

where $B(\mathbf{x})$ represents the motion-blurred image at pixel coordinate $\mathbf{x} \in \mathbb{R}^2$, and $I_t(\mathbf{x})$ corresponds to the radiance intensity captured at moment t .

To learn accurate 3D representations from motion-blurred images, BAD-NeRF proposes linearly interpolating camera poses in $\text{SE}(3)$ between the initial pose $\mathbf{T}_{\text{start}}$ at the exposure start and the final pose \mathbf{T}_{end} at the exposure end, generating sampled moments.:

$$\mathbf{T}_t = \mathbf{T}_{\text{start}} \cdot \exp \left(\frac{t}{n} \cdot \log(\mathbf{T}_{\text{start}}^{-1} \cdot \mathbf{T}_{\text{end}}) \right) \quad (14)$$

At each sampled moment, NeRF renders a sharp image. The predicted motion-blurred image is obtained by averaging all rendered images across moments. The loss between this predicted image and the real captured one is computed to jointly optimize NeRF network, T_{start} , and T_{end} , minimizing the discrepancy between predicted and real motion blur.

In-scattering Lightpath Model

In-scattering Lightpath Model (ISLM) decomposes complex lightpaths based on physical principles and unifies them as light scattering. While multiple scattering is overly complex and unnecessary for our purposes, we focus on single in-scattering and simulate six common ways of light transportation using this model, see Figure 6.

1. **Specular Reflection.** When light encounters a smooth surface (e.g., water, mirrors), its path reflects to form a polygonal path rather than a straight line before entering the camera.
2. **Refraction.** Light refracts when propagating between different media (e.g., observing underwater objects from the shore), altering its direction and causing a deviation in object’s position.
3. **Reflection+Refraction.** For instance, observing an underwater object alongside its reflected counterpart involves light paths combining reflection and refraction, where both paths converge to form the incident ray.
4. **Reflection+Transmission.** When viewing objects behind glass alongside their reflections (e.g., glass surfaces), the incident light combines reflected and transmitted paths. Transmission through thin glass can be approximated as straight-line propagation, while thicker glass necessitates refraction modeling.
5. **Glossiness.** A hybrid between specular and diffuse reflection, this phenomenon manifests as view-dependent highlights on surfaces like whiteboards or metals, where brightness varies with the observer’s angle.
6. **Diffusion.** Resulting from microscopic scattering, diffuse reflection aggregates light contributions from multiple directions, forming the incident ray observed at a pixel. This covers all non-specular surfaces encountered in daily observations.

All six scenarios can be unified as in-scattering, where light scatters at a single point on a medium or surface, with multiple scattered rays converging into the camera’s incident path to form a pixel.

Appendix B

Intuitive results of two scattering designs: 1) emitting five rays from a single primary sampling point, versus 2) emitting one scattering ray from each of five adjacent primary points. Emitting rays from five consecutive primary points outperforms the single-point multi-ray style, please see Figure 7 for details.

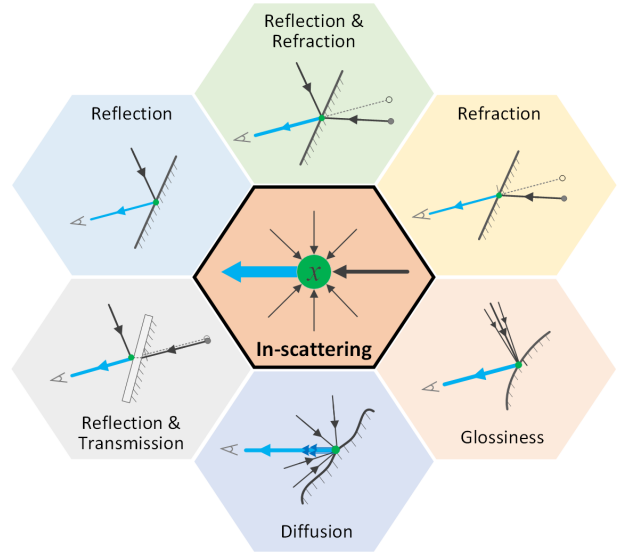


Figure 6: The in-scattering model of lightpaths.

Appendix C

The intuitive results of ablation studies by removing ISLM module from training and rendering, respectively. Please see Figure 8 for details.

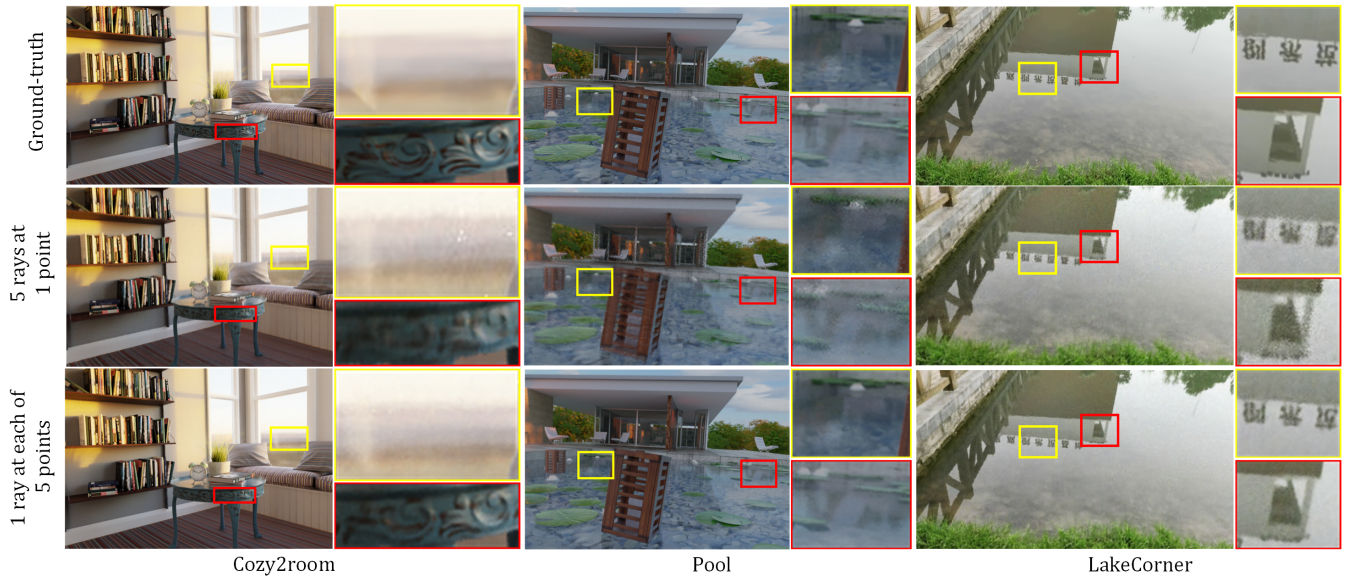


Figure 7: The intuitive comparisons of two scattering designs: 1) emitting five scattering rays from one primary sampling point, 2) emitting one scattering ray from each of five adjacent primary points. For example scenes of Deblur-dataset (Cozy2room and Pool) and self-captured dataset (LakeCorner), the second design evidently achieves better quality of synthesis images. The first design generates obvious noises while the second style captures more clearer details and handles light scatterings better (e.g. reflections on the water surface of Pool and LakeCorner, similar to ground-truth).

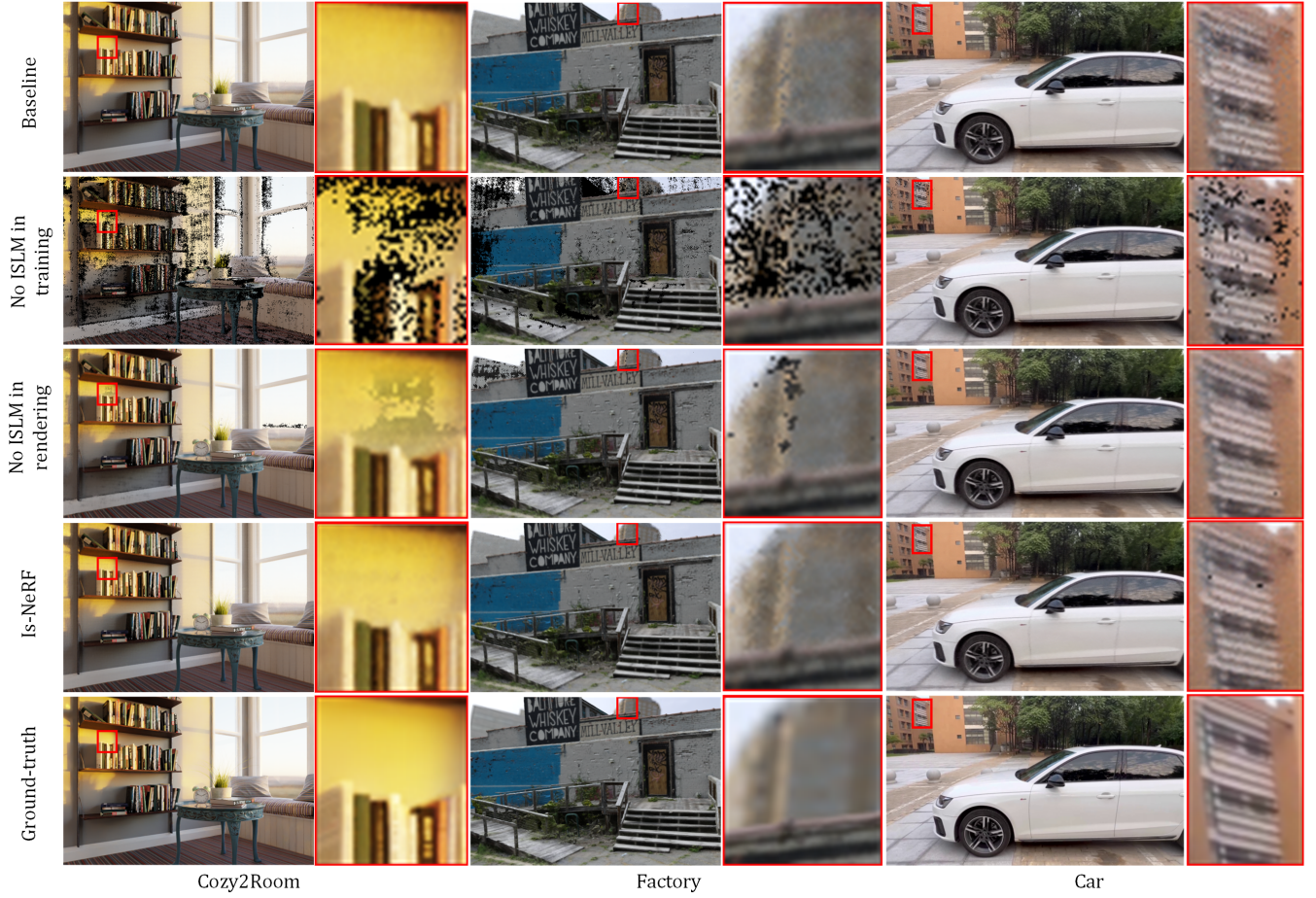


Figure 8: The intuitive results of ablation studies. By removing ISLM module from training, no available scatterings will be learned and then conducting scattering-aware volume rendering causes obvious data deficiency in the synthesis image of all three scenes (Cozy2room, Factory, and Car). While removing ISLM module from rendering leads to fewer flaws. By integrating ISLM in both training and rendering phases, our Is-NeRF significantly improves the quality of novel view images, superior to the baseline method.